atoms

MDPI

Article

MCDHF Calculations of Isotope Shifts for Be-like Ions Using Perturbation Theory and Finite-Field Method

Haoran Lin [1], Sijie Wu [1], Ran Si [1,*], Per Jönsson [2] and Chongyang Chen [1]

[1] Shanghai EBIT Laboratory, Key Laboratory of Nuclear Physics and Ion-Beam Application, Institute of Modern Physics, Department of Nuclear Science and Technology, Fudan University, Shanghai 200433, China; 25110200016@m.fudan.edu.cn (H.L.); 23110200026@m.fudan.edu.cn (S.W.); chychen@fudan.edu.cn (C.C.)
[2] Department of Materials Science and Applied Mathematics, Malmö University, SE-20506 Malmö, Sweden; per.jonsson@mau.se
* Correspondence: rsi@fudan.edu.cn

Abstract

In this work, we implement the finite-field (FF) method for isotope shift (IS) calculations within the relativistic multiconfiguration Dirac–Hartree–Fock (MCDHF) framework of the GRASPG program package. The implementation is benchmarked using the ten lowest-lying fine-structure levels of B II by comparing FF results for the IS parameters with first-order perturbation theory (PT) results obtained using the RIS4 program. The relative deviations for the IS parameters are within 0.03%, and the computed transition isotope shifts agree with previous theoretical predictions and experimental measurements within the reported experimental uncertainties. Additional calculations for Ar XV further confirm the consistency between the FF and PT methods for heavier ions, and the resulting isotope shifts are consistent with the experimental values. This implementation therefore provides GRASPG with two equivalent and reliable approaches for isotope shift calculations.

Keywords: MCDHF; GRASPG; isotope shift

1. Introduction

The study of isotope shifts (IS) is important for both fundamental and applied science [1–3]. The IS can be factorized into an electronic component and a nuclear contribution. Consequently, precise calculations of the electronic parameters are essential for accurately characterizing nuclear properties and, through deviations from linearity in King plots, for probing possible new physics beyond the Standard Model [4–8]. At the same time, isotope shifts provide stringent benchmarks for atomic structure methods, testing the accuracy of state-of-the-art approaches that incorporate relativistic effects, electron correlation, and quantum electrodynamic corrections.

There are several methods for calculating the electronic parameters of IS, such as the finite-field (FF) method, the analytical response (AR) method, and the first-order perturbation theory (PT) method (see the recent review paper [9]). Prior studies using the GRASP family of codes, which are based on multi-configuration Dirac–Hartree–Fock (MCDHF) and relativistic configuration interaction (RCI) theory, have predominantly relied on the first-order PT method implemented in the RIS4 package [10] to calculate the IS parameters. Recently, Lu et al. [11] implemented the FF method in the GRASP2018 program, demonstrating excellent agreement between the PT and FF methods. However, the relativistic coupled-cluster (RCC)-based FF approach demonstrated higher accuracy in calculating isotope shift parameters than the MCDHF-based PT method [12]. The consistency of the

Check for updates

Academic Editor: Ulrich D. Jentschura

Received: 27 May 2026
Revised: 7 July 2026
Accepted: 9 July 2026
Published: 13 July 2026

Copyright: © 2026 by the authors. Licensee MDPI, Basel, Switzerland. This article is an open access article distributed under the terms and conditions of the Creative Commons Attribution (CC BY) license.

PT and FF approaches remains an unresolved issue worthy of further systematic investigation, which will help improve the predictive capability of atomic spectroscopy in nuclear structure studies.

The FF approach requires multiple RCI calculations to obtain the relevant electronic parameters. This computational demand can be significantly reduced by the GRASPG program package [13], which offers substantial advantages over previous GRASP packages in terms of both computational time and memory requirement for RCI calculations. Therefore, in the present study, we extended the FF method to the GRASPG package.

The study of isotope shifts in B II holds a unique position in nuclear physics, astrophysics, and atomic physics [14,15]. Specifically, it can provide an exceptional platform to study the transition from proton-halo to neutron-halo structures, offering a stringent test for nuclear structure models [16]. The relative abundance of the two B isotopes, ^{10}B and ^{11}B, is expected to provide valuable information about the cosmic production of the light elements [17,18]. Additionally, the $2s^2\ ^1S_0$–$2s2p\ ^3P_0$ transition in B II has been proposed for building a high-precision optical atomic clock [19]. In this work, employing B II as the primary Be-like benchmark, we use the FF method to compute its isotope shifts and systematically compare the results with those obtained via the PT method. This comparative analysis allows us to evaluate the performance of the two methods within the MCDHF framework and to provide accurate isotope shift parameters for B II.

Ar XV provides a complementary heavier benchmark in the same Be-like isoelectronic sequence. Compared with B II, its larger nuclear charge enhances relativistic and finite-nuclear-size effects. In addition, the isotope shift in the $2s2p\ ^3P_1$–$2s2p\ ^3P_2$ fine-structure transition in Be-like argon has available experimental and high-precision theoretical data [20,21]. Therefore, Ar XV is well suited for testing whether the agreement between the FF and PT approaches remains robust beyond the light B II ion.

2. Theoretical Methods

2.1. Multiconfiguration Dirac Hartree Fock Method

The MCDHF method and calculation of isotope shift have been thoroughly described in studies such as Refs. [10,22,23], so we will only provide a brief description here. In the MCDHF method, the atomic state wave function (ASF) is expressed as a linear combination of symmetry-adapted configuration state functions (CSFs):

$$\Psi(\gamma PJM_J) = \sum_{i}^{N_{CSFs}} c_i \Phi(\gamma_i PJM_J), \tag{1}$$

where N_{CSFs} is the number of CSFs, P is the parity, γ_i represents other quantum numbers of the corresponding states, J represents the total angular momenta, M_J is the angular momentum projection on J, and c_i is the mixing coefficient.

The one-electron Dirac orbitals used to construct the CSFs and mixing coefficients c_i are obtained by iteratively solving the self-consistent field (SCF) equations of the weighted energy functional based on the Dirac–Coulomb Hamiltonian:

$$H_{\mathrm{DC}} = \sum_{j=1}^{N} (c\boldsymbol{\alpha}_j \cdot \boldsymbol{p}_j + (\boldsymbol{\beta}_j - 1)c^2 + V(r_j)) + \sum_{j<k}^{N} \frac{1}{r_{jk}}, \tag{2}$$

where $V(r_j)$ is the monopole part of the electron–nucleus Coulomb interaction, r_{jk} is the distance between electrons j and k, $\boldsymbol{\alpha}$ and $\boldsymbol{\beta}$ are the Dirac matrices, N is the number of electrons, $\boldsymbol{p}_j$ is the momentum operator of electron j and c is the speed of light.

The Breit interaction and leading QED corrections (vacuum polarization and self-energy) are included in subsequent relativistic configuration interaction (RCI) calculations.

2.2. Configuration State Function Generator

As mentioned in the previous subsection, the MCDHF/RCI method expresses ASFs as expansions over CSFs built on one-electron Dirac orbitals. As the number of orbitals grows to accurately capture electron correlation, the number of matrix elements increases dramatically, making the construction of the Hamiltonian extremely demanding in terms of both time and memory. In this process, spin-angular integration constitutes the dominant computational cost. To alleviate this computational load, the Configuration State Function Generator (CSFG) approach was introduced [24]. The key insight is that spin-angular integration depends on orbital symmetries, but not on their principal quantum numbers. CSFGs exploit this by dividing the CSF space into the following:

1. Labeling space: CSFs generated by excitations (single, double, triple, quadruple—SDTQ, etc.) from a multireference (MR) configuration to a labeling-ordered set of highly occupied orbitals. These CSFs account for dominant correlation effects, near-degeneracies, and long-range rearrangements.
2. Correlation space: CSFs obtained by SD excitations from the MR configuration to a symmetry-ordered (SO) set of correlation orbitals. This space captures short-range dynamical correlation and is typically much larger than the labeling space.

A CSFG is defined as a generating CSF with orbitals in the SO set at their highest principal quantum number. From a single CSFG, a group of CSFs is generated by de-exciting the SO orbital(s) to lower principal quantum numbers, while keeping all spin-angular coupling quantum numbers unchanged.

Once the spin-angular integration between two CSFGs is computed, the resulting spin-angular coefficients are stored. For any pair of CSFs obtained by de-exciting the symmetry-ordered (SO) orbitals in the two CSFGs to lower principal quantum numbers, the corresponding spin-angular integration is then obtained directly by reusing the same spin-angular coefficients. This avoids repeated spin-angular integrations and significantly reduces the computational load. Therefore, this methodology retains the accuracy of the conventional CSF expansion while drastically reducing the computational load.

2.3. Isotope Shift

Isotope shifts consist of two components: the mass shift (MS), arising from the difference in nuclear mass between isotopes, and the field shift (FS), originating from the difference in nuclear volume. The mass shift further divides into the normal mass shift (NMS), which results from the change in reduced mass between isotopes, and the specific mass shift (SMS), which stems from momentum correlations in the many-electron system. The field shift, on the other hand, arises from the extended nature of the nucleus, which causes the electrostatic potential to deviate from the Coulomb potential of a point charge Z. In the GRASPG package, this effect is accounted for by introducing a nucleus potential based on a Fermi charge distribution.

Let E denote the energy level and A, A', M_A, $M_{A'}$ represent the mass numbers and nuclear masses of two isotopes, respectively. In leading order, the isotope shift of a level i can then be expressed:

$$\delta E_i^{A,A'} = \delta E_{i,\mathrm{FS}}^{A,A'} + \delta E_{i,\mathrm{MS}}^{A,A'} = F_i \delta\langle r^2\rangle + K_i \frac{M_A - M_{A'}}{M_A M_{A'}}. \tag{3}$$

Here, F and $K = K_{\mathrm{NMS}} + K_{\mathrm{SMS}}$ are the field shift and mass shift factors, respectively, and $\delta\langle r^2\rangle$ represents the nuclear mean-square radius (rms) difference value between two isotopes.

2.3.1. Mass Shift

The relativistic forms of NMS and SMS operators, up to the order of $(\alpha Z)^2$, can be expressed as follows [10]:

$$\hat{H}_{\mathrm{NMS}} = \frac{1}{2M}\sum_{j=1}^{N}\left(\mathbf{p}_j^2 - \frac{\alpha Z}{r_j}\boldsymbol{\alpha}_j\cdot\mathbf{p}_j - \frac{\alpha Z}{r_j}(\boldsymbol{\alpha}_j\cdot\mathbf{C}_j^1)\mathbf{C}_j^1\cdot\mathbf{p}_j\right) \tag{4}$$

$$\hat{H}_{\mathrm{SMS}} = \frac{1}{2M}\sum_{j\neq k}^{N}\left(\mathbf{p}_j\cdot\mathbf{p}_k - \frac{\alpha Z}{r_j}\boldsymbol{\alpha}_j\cdot\mathbf{p}_k - \frac{\alpha Z}{r_j}(\boldsymbol{\alpha}_j\cdot\mathbf{C}_j^1)\mathbf{C}_j^1\cdot\mathbf{p}_k\right). \tag{5}$$

Within the framework of the first-order perturbation theory, we compute the expectation values of the MS operators to obtain the MS factors:

$$\frac{K_{i,\mathrm{NMS}}}{M} = \langle\Psi_i(\gamma PJM_J)|\hat{H}_{\mathrm{NMS}}|\Psi_i(\gamma PJM_J)\rangle \tag{6}$$

$$\frac{K_{i,\mathrm{SMS}}}{M} = \langle\Psi_i(\gamma PJM_J)|\hat{H}_{\mathrm{SMS}}|\Psi_i(\gamma PJM_J)\rangle. \tag{7}$$

In the finite-field method, the MS factors are determined using an effective Hamiltonian $\hat{H}_{\mathrm{eff}} = \hat{H} + \lambda_0\hat{O}_{\mathrm{NMS/SMS}}$, where λ_0 is a scaling parameter and $\hat{O}_{\mathrm{NMS/SMS}}$ are the M independent parts of NMS/SMS operators defined in Equations (4) and (5). Thus, the MS factors are extracted as [9]

$$K_{i,\mathrm{SMS/NMS}} = \left.\frac{\partial E_i}{\partial\lambda}\right|_{\lambda_0=0} \approx \frac{E_i(+\lambda_0) - E_i(-\lambda_0)}{2\lambda_0} \tag{8}$$

where $E_i(\pm\lambda_0)$ represents the calculated total energies at the $\pm\lambda_0$ values using the Hamiltonian $\hat{H}_{\mathrm{eff}}$. Here, we have adopted $\lambda_0 = 10^{-5}$ a.u. for all calculated levels.

2.3.2. Field Shift

Adopting the electronic density $\rho(\mathbf{r})$ for the zeroth-order picture, perturbation theory yields the first-order FS:

$$\delta E_{i,FS}^{A,A'} = -\int_{\mathbb{R}^3}\left[V^A(\mathbf{r}) - V^{A'}(\mathbf{r})\right]\rho_i(\mathbf{r})\,d^3\mathbf{r}, \tag{9}$$

where $V^A(\mathbf{r})$ and $V^{A'}(\mathbf{r})$ are the potentials arising from the nuclear charge distributions of the two isotopes and $\rho_i(\mathbf{r})$ is the electron density of level i of the reference isotope. Assuming a spherical nuclear charge distribution and expanding the electron density within the nucleus as a polynomial

$$\rho_i(\mathbf{r}) \approx b(r) = b_{i,0} + b_{i,2}r^2 + b_{i,4}r^4 + b_{i,6}r^6 \tag{10}$$

the field shift can be written as

$$\delta E_{i,FS}^{A,A'} \approx F_{i,0}\delta\langle r^2\rangle + F_{i,2}\delta\langle r^4\rangle + F_{i,4}\delta\langle r^6\rangle + F_{i,6}\delta\langle r^8\rangle. \tag{11}$$

Neglecting the variation in electron density over the nuclear volume, $\rho_i(\mathbf{r})$ can be replaced with the value at $\mathbf{r} = \mathbf{0}$; the energy shift then becomes

$$\delta E_{i,\mathrm{FS}} = \frac{2\pi}{3}Z\rho_i(\mathbf{0})\delta\langle r^2\rangle. \tag{12}$$

From the above derivation, the FS factor can be deduced to be

$$F_{i,0} = +\frac{2\pi}{3}Z\rho_i(\mathbf{0}). \tag{13}$$

To account for the varying electron density (VED) inside the nucleus, the level electronic factor $F_{i,0}^{\mathrm{VED}}$ is introduced by rewriting the expression for the field shift

$$\begin{aligned}\delta E_{i,\mathrm{FS}} &\approx \left(F_{i,0} + F_{i,2}\frac{\delta\langle r^4\rangle}{\delta\langle r^2\rangle} + F_{i,4}\frac{\delta\langle r^6\rangle}{\delta\langle r^2\rangle} + F_{i,6}\frac{\delta\langle r^8\rangle}{\delta\langle r^2\rangle}\right)\delta\langle r^2\rangle \\ &= \left(F_{i,0}^{(0)\mathrm{VED}} + F_{i,0}^{(1)\mathrm{VED}}\delta\langle r^2\rangle\right)\delta\langle r^2\rangle\end{aligned} \tag{14}$$

where $F_{i,0}^{(0)\mathrm{VED}}$ and $F_{i,0}^{(1)\mathrm{VED}}$, the expressions for which can be found in Equations (47) and (48) in [10], are the FS factors that account for the varying electron density within the nuclear volume. Because $F_{i,0}^{(1)\mathrm{VED}}$ is several orders of magnitude smaller than $F_{i,0}^{(0)\mathrm{VED}}$, we neglect $F_{i,0}^{(1)\mathrm{VED}}$ here.

In the finite-field method, the λ_0 parameter in Equation (8) corresponds to a change in the rms charge radius. Thus, the finite-field method reduces to the calculation of the following derivative [9]:

$$F_{i,0} = -\frac{E_i\left(\langle r_0^2\rangle + h\right) - E_i\left(\langle r_0^2\rangle - h\right)}{2h}. \tag{15}$$

Here, h denotes a small change in the mean-squared charge radius. Because we employ a Fermi-distributed nuclear charge, the VED inside the nucleus is automatically taken into account in this approach.

3. Results and Discussion

3.1. B II

For B II, we target the 10 levels belonging to the $1s^22s^2$, $1s^22s2p$ and $1s^22p^2$ configurations. The restricted active set approach (RAS) method [25] is used to generate the CSF list.

In the MCDHF procedure, the $1s^2nln'l'$ configurations with $2 \le n \le n' \le 3$ and $0 \le l \le l' \le 2$ define the multireference (MR) set for levels of both parities. The valence electrons in the MR configurations are allowed to be singly and doubly (SD) excited to active sets listed in Table 1 layer by layer; therefore, the valence–valence (VV) electron correlation effect is taken into account. In the initial calculation, to better describe the $1s, 2s, 2p$ spectroscopic orbitals, the $3s, 3p, 3d$ orbitals are optimized together with them. Subsequently, the active set is systematically enlarged in order to monitor the convergence of computed properties. At each step, only the newly added layer of orbitals is optimized, while the previously obtained orbitals are kept fixed.

Table 1. Layers of correlation orbitals, in nonrelativistic notation, undertaken in the MCDHF/RCI method to carry out calculations of different atomic properties.

Active Sets	Orbitals
AS1	$\{4s, 4p, 4d, 4f\}$
AS2	$\{5s, 5p, 5d, 5f, 5g\}$
AS3	$\{6s, 6p, 6d, 6f, 6g, 6h\}$
AS4	$\{7s, 7p, 7d, 7f, 7g, 7h, 7i\}$
AS5	$\{8s, 8p, 8d, 8f, 8g, 8h, 8i\}$
AS6	$\{9s, 9p, 9d, 9f, 9g, 9h, 9i\}$
AS7	$\{10s, 10p, 10d, 10f, 10g, 10h, 10i\}$
AS8	$\{11s, 11p, 11d, 11f, 11g, 11h, 10i\}$
AS9	$\{12s, 12p, 12d, 12f, 12g, 11h, 10i\}$
AS10	$\{13s, 13p, 13d, 13f, 12g, 11h, 10i\}$
AS11	$\{14s, 14p, 14d, 13f, 12g, 11h, 10i\}$
AS12	$\{15s, 15p, 14d, 13f, 12g, 11h, 10i\}$

In the RCI procedure, the MR set is enlarged to include all the $1s^2nln'l'$ configurations with $2 \leq n \leq n' \leq 4$ and $0 \leq l \leq l' \leq 3$. In addition, not only are the valence electrons allowed to be SD-excited to generate the CSFs expansion, which includes the core–valence (CV) and core–core (CC) correlations, but so are the $1s$ core electrons.

3.1.1. Energy Levels

In Figure 1, we show the convergence of our calculated excitation energies as a function of increasing active set (AS). As illustrated, the excitation energies between AS_{11} and AS_{12} are found to agree within 1.7 cm^{-1} (0.002%), indicating that a high level of convergence is achieved in our calculations.

In Table 2, we compare our calculated excitation energies with the compiled values of the National Institute of Standards and Technology (NIST) Atomic Spectra Database (ASD) [26], as well as with the previous MCDHF/RCI calculations [27–29]. Compared with the NIST values, the relative deviations are within 0.02% except for $2s2p\ ^1P_1$ (0.04%) and $2p^2\ ^1S_0$ (0.03%). The reason for the latter deviations can be traced to the slow convergence of the $2s2p$ and $2p^2$ singlet level energies with respect to the l quantum numbers in the orbital basis; for example, see [30], chapter 5. Further improvements of excitation energies would require extrapolations with respect to l [31].

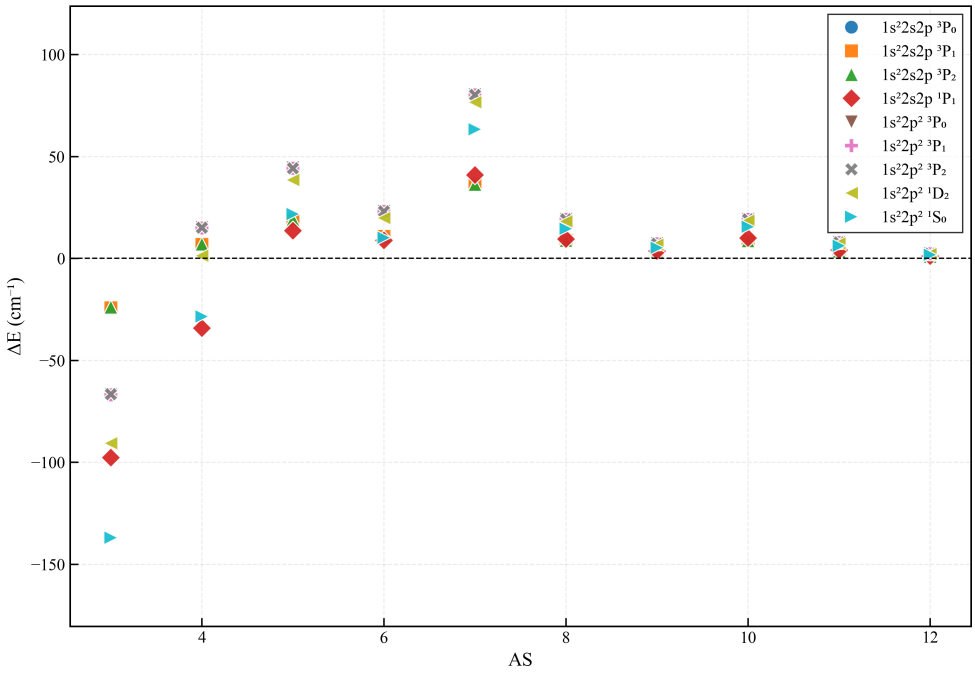


Figure 1. Convergence for excitation energies with enlarging active set (AS), where ΔE represents the energy change between AS_{n-1} and AS_n.

Table 2. The present excitation energies of B II calculated using the MCDHF/RCI method compared with NIST ASD values [26] and previous theoretical calculations [27–29] in cm^{-1}. The last column represents the relative deviation between the present calculations and the NIST values.

Atomic Levels [1]	This Work	Prev. Calc. [27]	Prev. Calc. [28]	Prev. Calc. [29]	NIST [26]	Relative Difference
$2s^2\ ^1S_0$	0	0	0	0	0	0
$2s2p\ ^3P_0$	37,330.21	37,271.86		37,326	37,335.54	0.01%
$2s2p\ ^3P_1$	37,335.58	37,277.92		37,331	37,341.65	0.02%
$2s2p\ ^3P_2$	37,351.65	37,293.97		37,347	37,357.80	0.02%
$2s2p\ ^1P_1$	73,426.76	73,494.38	73,655	73,670	73,396.51	0.04%

Table 2. *Cont.*

Atomic Levels [1]	This Work	Prev. Calc. [27]	Prev. Calc. [28]	Prev. Calc. [29]	NIST [26]	Relative Difference
$2p^2\ ^3P_0$	98,908.42	98,889.85		98,911	98,911.38	0.00%
$2p^2\ ^3P_1$	98,916.07	98,898.43		98,919	98,919.87	0.00%
$2p^2\ ^3P_2$	98,928.94	98,911.77		98,932	98,933.26	0.00%
$2p^2\ ^1D_2$	102,375.20	102,401.85	102,431	102,588	102,362.77	0.01%
$2p^2\ ^1S_0$	127,702.92	127,540.87	127,923	127,854	127,661.19	0.03%

[1] In the notation of atomic levels, only the valence–shell electrons are explicitly denoted, with the core electrons $1s^2$ omitted but implied.

3.1.2. Isotope Shift

The PT-based IS calculations are performed using the RIS4 program package [10]. To perform the FF-based IS calculations using the GRASPG [13] package, we incorporated the NMS and SMS operators into the RCI program. Analogously to the caching mechanism for the `rci.res` file in the GRASPG package (see Section 3.4 in [13]), we store the contributions from other effects in the RCI calculation, and then add or subtract the NMS contribution, saving the results in the dedicated files `nms1.res` and `nms2.res`, respectively. The same procedure is applied to SMS. We then differentiate the NMS and SMS contributions to derive the K_{NMS} and K_{SMS} factors. A perturbation parameter of $\lambda_0 = 10^{-5}$ a.u. is adopted. The FS parameter is obtained by applying finite differences to the RMS radius input parameter; the perturbation parameter ($h = 0.0217$ fm) is chosen to be the difference in RMS radii between ^{10}B and ^{11}B [32]. Test calculations have shown that the IS electronic factors are insensitive to the choice of λ_0 and h values. Varying λ_0 from 10^{-4} to 10^{-6} has only changed the SMS and NMS factors by less than 10^{-7}, while varying h from 0.001 to 0.1 fm leaves all significant digits of the FS factors unchanged. A convergence study is also carried out for the IS parameters, yielding differences of 0.014%, 0.005%, and 0.007% for the NMS, SMS, and FS factors between the AS_{11} and AS_{12} calculations, respectively. The NMS, SMS and FS electronic parameters calculated by the PT and FF methods from AS_{12} are presented in Table 3 and compared with previous calculations employing the MCDHF/RCI + PT method [18,27]. In particular, we present two types of PT-calculated FS parameters; one neglects the varying density inside the nucleus, while the other includes this effect.

As shown in Table 3, the NMS and SMS parameters calculated via the PT and FF methods are nearly identical in terms of the present significant digits. For the FS parameters, the VED effect contributes 0.05% to the results. Consequently, our PT-based FS parameters that incorporate this effect exhibit better agreement with the FF results, in which the VED effect is inherently included, and the agreement is mostly within 0.03%. Although the VED effect only contributes 0.05% to the FS parameters for B II, it could become substantially larger for heavy ions, where the nucleus has a much larger size.

Since the previous calculations [18,27] did not include the VED effect, their FS factors agree better with our PT-based results without the VED effect, with average deviations of about 0.3%. For the NMS factor, the average deviation is 1%, and for the SMS factor, the average deviation is 0.2%, with the exception of the $2s2p\ ^1P_1$–$2p^2\ ^1S_0$ transition (6.4%). The large discrepancy in this transition is primarily attributed to SMS, which is a two-body operator and highly sensitive to electron correlation effects. This sensitivity is particularly pronounced for the upper level of this transition ($2p^2\ ^1S_0$) because it exhibits strong mixing with other states. As shown in Table 1, our calculated energy levels, particularly for $2p^2\ ^1S_0$, are in considerably better agreement with experimental data than previous theoretical results. This improvement indicates that our approach captures electron correlation effects

more comprehensively, and consequently lends support to the reliability of our calculated isotope shift parameters.

Table 3. Electronic parameters for field shift (FS), normal mass shift (NMS), and specific mass shift (SMS) for selected transitions in Be-like B II.

Transition	Field Shift (MHz fm^{-2})				NMS (GHz amu)			SMS (GHz amu)		
	FF	PT (VED)	PT	Prev. Calc. [1]	FF	PT	Prev. Calc. [1]	FF	PT	Prev. Calc. [1]
$2s^2\ ^1S_0$–$2s2p\ ^1P_1$	−44.379	−44.366	−44.389	−44.427 [a] −44.467 [b]	1207.04	1206.99	1183.04 [a] 1205.97 [b]	1173.49	1173.54	1174.99 [a] 1175.20 [b] 1162.07 [c]
$2s2p\ ^3P_1$–$2p^2\ ^3P_2$	−48.287	−48.283	−48.308	−48.308 [a]	1011.67	1011.62	1015.71 [a]	1471.79	1471.83	1468.19 [a] 1468.88 [c]
$2s2p\ ^3P_0$–$2p^2\ ^3P_1$	−48.285	−48.280	−48.305	−48.307 [a]	1011.71	1011.70	1015.89 [a]	1471.18	1471.22	1467.78 [a] 1468.88 [c]
$2s2p\ ^3P_1$–$2p^2\ ^3P_1$	−48.294	−48.288	−48.313	−48.309 [a]	1012.24	1012.23	1015.71 [a]	1471.06	1471.10	1467.39 [a] 1468.88 [c]
$2s2p\ ^3P_2$–$2p^2\ ^3P_2$	−48.290	−48.285	−48.310	−48.308 [a]	1011.95	1011.90	1015.71 [a]	1471.14	1471.18	1467.44 [a] 1468.88 [c]
$2s2p\ ^3P_1$–$2p^2\ ^3P_0$	−48.299	−48.296	−48.320	−48.310 [a]	1012.60	1012.55	1016.27 [a]	1470.87	1470.91	1467.04 [a] 1468.88 [c]
$2s2p\ ^3P_2$–$2p^2\ ^3P_1$	−48.297	−48.290	−48.315	−48.312 [a]	1012.52	1012.51	1016.46 [a]	1470.41	1470.45	1466.64 [a] 1468.88 [c]
$2s2p\ ^1P_1$–$2p^2\ ^1S_0$	−23.945	−23.951	−23.963	−23.316 [a]	894.09	894.06	907.85 [a]	573.52	573.66	536.91 [a] 520.99 [c]
$2s2p\ ^1P_1$–$2p^2\ ^1D_2$	−38.435	−38.431	−38.450	−38.631 [a]	475.63	475.57	492.27 [a]	2459.73	2459.63	2460.51 [a] 2464.59 [c]

[1] 'a', 'b' and 'c' are taken from Refs. [27], [18] and [28] respectively.

In Table 4, we compare our calculated IS for ^{10}B relative to ^{11}B using the FF and PT methods with previous theoretical [18,27,28,33] and experimental results [28,34]. It can be seen that our calculated IS using the two methods are almost the same in the present significant digits. In addition, all the theoretical values fall within the corresponding experimental uncertainties. Although the experimental uncertainties are substantial, our theoretical results consistently lie within the overlapping range shared by the various experiments, lending credibility to our calculations. For example, for the $2s2p\ ^3P_1$–$2p^2\ ^3P_2$ transition, the two experimental values are 21,600(3600) and 24,000(3600) MHz, respectively. Our calculations values 22,435 (PT) and 22,434 (FF) MHz both fall with their common range of 20,400–25,200 MHz; for the $2s2p\ ^3P_2$–$2p^2\ ^3P_2$ transition, the two experimental values are 21,600(4500) and 18,300(4500) MHz, respectively, and our calculations values 22,431 (PT) and 22,431 (FF) Mhz also lie with the overlapping interval of 17,100–22,800 MHz.

Table 4. Isotope shifts in MHz for ^{10}B with respect to ^{11}B. The nuclear masses of the two isotopes are taken from Ref. [35].

Transitions	FF	PT	Prev. Calc. [1] [18]	Prev. Calc. [27]	Prev. Calc. [33]	Prev. Calc. [1] [28]	Expt. [34]	Expt. [28]
$2s^2\ ^1S_0$–$2s2p\ ^1P_1$	21,505	21,505	21,525	21,320	21,303(66)	21,420	21,000(3000)	21,000(3000)
$2s2p\ ^3P_1$–$2p^2\ ^3P_2$	22,435	22,434		22,449	22,369(170)	22,439	21,600(3600)	24,000(3600)
$2s2p\ ^3P_0$–$2p^2\ ^3P_1$	22,429	22,430			22,370(170)		21,600(3600)	21,600(3600)
$2s2p\ ^3P_1$–$2p^2\ ^3P_1$	22,433	22,433			22,349(170)		21,600(6900)	21,600(6900)
$2s2p\ ^3P_2$–$2p^2\ ^3P_2$	22,431	22,431			22,371(170)		21,600(4500)	18,300(4500)
$2s2p\ ^3P_1$–$2p^2\ ^3P_0$	22,435	22,435			22,372(170)		21,600(3600)	21,600(3600)
$2s2p\ ^3P_2$–$2p^2\ ^3P_1$	22,430	22,430			22,372(170)		21,600(3600)	21,600(3600)
$2s2p\ ^1P_1$–$2p^2\ ^1S_0$	13,258	13,259		14,327	12,689(580)	12,780		12,600(1200)
$2s2p\ ^1P_1$–$2p^2\ ^1D_2$	26,519	26,517		26,677	26,663(55)	26,592		26,600(100)

[1] Although Refs. [18,28] only give the mass shift of the transition, we treat the mass shift as an approximation of the total isotope shift.

3.2. Ar XV

The calculations for Ar XV are performed using the same approach as for B II, but with the active set restricted to AS_9. As illustrated below, this restriction is sufficient for higher-charged ions, where electron correlation converges more rapidly.

3.2.1. Energy Levels

Our calculated excitation energies for the first 10 levels have been converged to within 0.003% as the active set is enlarged. The final results are listed in Table 5, alongside the NIST ASD values [26] and earlier theoretical calculations [27]. Except for $2s2p\ ^1P_1$ (0.04%) and $2p^2\ ^1S_0$ (0.03%), all relative deviations from NIST are within 0.02%.

Table 5. Excitation energies of Be-like Ar XV obtained in the present MCDHF/RCI calculation, compared with the previous MCDHF/RCI calculation of Nazé et al. [27] and the NIST ASD values [26]. Energies are given in cm^{-1} relative to the $1s^22s^2\ ^1S_0$ ground level. The last column gives the relative difference between the present results and NIST. The core configuration $1s^2$ is omitted in the level labels.

Atomic Levels	This Work	Prev. Calc. [27]	NIST [26]	Relative Difference
$2s^2\ ^1S_0$	0	0	0	0
$2s2p\ ^3P_0$	228,693.49	228,682.17	228,684	0.00%
$2s2p\ ^3P_1$	235,874.74	235,864.98	235,860.182	0.01%
$2s2p\ ^3P_2$	252,699.11	252,691.31	252,679.553	0.01%
$2s2p\ ^1P_1$	452,380.55	452,526.02	452,182	0.04%
$2p^2\ ^3P_0$	605,101.34	605,165.94	604,917	0.03%
$2p^2\ ^3P_1$	615,077.70	615,141.91	615,140	0.01%
$2p^2\ ^3P_2$	628,338.58	628,406.60	628,308	0.00%
$2p^2\ ^1D_2$	689,690.57	689,832.66		
$2p^2\ ^1S_0$	840,718.67	841,026.88	840,620	0.01%

3.2.2. Isotope Shift

In Table 6, we compare our calculated mass-shift (MS) and field-shift (FS) electronic parameters obtained using the PT and FF methods, along with other theoretical values [27]. The NMS and SMS factors calculated using the PT and FF approaches exhibit average agreements of 0.02% and 0.001%, respectively. For the field-shift factors, the VED effect is much larger than that in B II, contributing 0.46%. When the VED effect is taken into account, the FF and PT field-shift factors agree to within 0.06%.

Table 6. Electronic parameters for field shift (FS), normal mass shift (NMS), and specific mass shift (SMS) for selected transitions in Be-like Ar XV.

Transition	Field Shift ($GHz\ fm^{-2}$)				NMS (GHz amu)			SMS (GHz amu)		
	FF	PT (VED)	PT	Prev. Calc. [1]	FF	PT	Prev. Calc. [1]	FF	PT	Prev. Calc. [1]
$2s^2\ ^1S_0$–$2s2p\ ^1P_1$	−18.0568	−18.0468	−18.1290	−18.1155	7417.02	7415.64	7364.70	62,535.96	62,534.67	62,539.61
$2s2p\ ^3P_1$–$2p^2\ ^3P_2$	−19.2585	−19.2477	−19.3354	−19.3324	6369.80	6368.34	6379.50	67,580.50	67,580.69	67,575.14
$2s2p\ ^3P_0$–$2p^2\ ^3P_1$	−19.2552	−19.2443	−19.3320	−19.3291	6310.14	6308.68	6320.30	67,501.30	67,501.50	67,496.00
$2s2p\ ^3P_1$–$2p^2\ ^3P_1$	−19.2472	−19.2363	−19.3240	−19.3210	6239.29	6237.83	6249.40	67,415.29	67,415.49	67,409.49
$2s2p\ ^3P_2$–$2p^2\ ^3P_2$	−19.2441	−19.2332	−19.3208	−19.3178	6187.06	6185.61	6196.90	67,376.50	67,376.70	67,370.67
$2s2p\ ^3P_1$–$2p^2\ ^3P_0$	−19.2043	−19.1936	−19.2811	−19.2780	6140.97	6139.52	6149.50	67,121.79	67,121.98	67,116.06
$2s2p\ ^3P_2$–$2p^2\ ^3P_1$	−19.2327	−19.2218	−19.3094	−19.3064	6056.55	6055.10	6066.80	67,211.29	67,211.50	67,205.02
$2s2p\ ^1P_1$–$2p^2\ ^1S_0$	−16.7233	−16.7139	−16.7901	−16.7924	6385.96	6384.72	6314.70	56,347.29	56,345.97	56,368.06
$2s2p\ ^1P_1$–$2p^2\ ^1D_2$	−18.3034	−18.2930	−18.3764	−18.3840	3882.26	3880.83	3900.70	68,030.22	68,029.69	68,033.30
$2s2p\ ^3P_1$–$2s2p\ ^3P_2$	−0.0145	−0.0145	−0.0145	−0.0146	182.74	182.73	182.60	204.00	203.99	204.47

[1] Previous calculations are taken from the MCDHF/RCI results of Nazé et al. [27].

As shown in Table 7, for the $2s2p\ ^3P_1$–$2s2p\ ^3P_2$ interval, the two methods differ by only 0.02 GHz amu in K_{MS}, corresponding to about 0.005%. The field-shift factors from two methods agree to within the significant digits. In addition, the mass-shift and field-shift factors obtain by the two methods and other previous data to within 0.15% and 1.7% on average, respectively. The isotope shift for $Ar^{40,36}$ derived from both the FF and PT methods is 0.001262 nm, which is consistent with previous theoretical values and also agrees with the experimental value of 0.00120(10) nm within its uncertainty.

Table 7. Total isotope-shift factors and wavelength isotope shift for the $2s2p\ ^3P_1$–$2s2p\ ^3P_2$ fine-structure transition in Be-like Ar XV. The mass-shift factor K_{MS} is given in GHz amu, the field-shift factor F in GHz fm^{-2}, and the wavelength isotope shift $\delta\lambda^{40,36}$ in nm, using ^{36}Ar as the reference isotope. The $\delta(r^2)$ and nuclear masses are from Refs. [32,35], respectively.

	PT	FF	Prev. Calc.	Experiment
K_{MS}	386.71	386.73	387.07 [27], 386.94 [21]	
F	−0.0145	−0.0145	−0.0146 [27], −0.0144 [21]	
$\delta\lambda^{40,36}$	0.001262	0.001262	0.00126 [27], 0.00122(5) [36]	0.00120(10) [36]

4. Conclusions

Utilizing MCDHF/RCI implemented in GRASPG, we performed ab initio calculations via the FF method and PT to determine the isotope shift parameters. Our results demonstrate that FF and PT yield essentially equivalent IS parameters within the same MCDHF/RCI framework, indicating that the discrepancy between the isotope shift parameters calculated by the FF and PT methods reported in previous studies does not originate from the methods themselves, but rather from the differences in the atomic state wavefunctions.

Given that GRASPG is capable of generating more accurate atomic wavefunctions than previous GRASP packages, we anticipate that the finite-field and perturbation theory methods used in this work will enable the determination of more precise isotope shift parameters in future investigations.

Author Contributions: Methodology, R.S. and P.J.; Software, H.L., S.W. and R.S.; Formal analysis, H.L.; Writing—original draft, H.L. and R.S.; Writing—review and editing, R.S., P.J. and C.C.; Supervision, C.C. and R.S. All authors have read and agreed to the published version of the manuscript.

Funding: This research was funded by National Key Research and Development Project of China (No. 2022YFA1602303 and No. 2022YFA1602500), the National Natural Science Foundation of China (No. 12074081 and No. 12104095), and Swedish Research Council (VR 2023-05367).

Data Availability Statement: The original contributions presented in this study are included in the article. Further inquiries can be directed to the corresponding author.

Acknowledgments: H.L., S.W., R.S. and C.C. acknowledge support from National Key Research and Development Project of China (No. 2022YFA1602303 and No. 2022YFA1602500) and the National Natural Science Foundation of China (No. 12074081 and No. 12104095). P.J. acknowledges support from the Swedish Research Council (VR 2023-05367).

Conflicts of Interest: The authors declare no conflicts of interest.

References

1. Berengut, J.C.; Flambaum, V.V.; Kozlov, M.G. Isotope shift calculations in Ti II. *J. Phys. B At. Mol. Opt. Phys.* **2008**, *41*, 235702. [CrossRef]
2. King, S.A.; Spieß, L.J.; Micke, P.; Wilzewski, A.; Leopold, T.; Benkler, E.; Lange, R.; Huntemann, N.; Surzhykov, A.; Yerokhin, V.A.; et al. An optical atomic clock based on a highly charged ion. *Nature* **2022**, *611*, 43–47. [CrossRef] [PubMed]

3. Peik, E.; Schumm, T.; Safronova, M.S.; Pálffy, A.; Weitenberg, J.; Thirolf, P.G. Nuclear clocks for testing fundamental physics. *Quantum Sci. Technol.* **2021**, *6*, 034002. [CrossRef]
4. Drake, G.W.F.; Nörtershäuser, W.; Yan, Z.C. Isotope shifts and nuclear radius measurements for helium and lithium. *Can. J. Phys.* **2005**, *83*, 311–325. [CrossRef]
5. Friar, J.L.; Martorell, J.; Sprung, D.W.L. Nuclear sizes and the isotope shift. *Phys. Rev. A* **1997**, *56*, 4579–4586. [CrossRef]
6. Mikami, K.; Tanaka, M.; Yamamoto, Y. Probing new intra-atomic force with isotope shifts. *Eur. Phys. J. C* **2017**, *77*, 896. [CrossRef]
7. Viatkina, A.V.; Yerokhin, V.A.; Surzhykov, A. Calculation of isotope shifts and King-plot nonlinearities in Ca^+. *Phys. Rev. A* **2023**, *108*, 022802. [CrossRef]
8. Counts, I.; Hur, J.; Aude Craik, D.P.L.; Jeon, H.; Leung, C.; Berengut, J.C.; Geddes, A.; Kawasaki, A.; Jhe, W.; Vuletić, V. Evidence for nonlinear isotope shift in Yb^+ search for new boson. *Phys. Rev. Lett.* **2020**, *125*, 123002. [CrossRef] [PubMed]
9. Sahoo, B.K.; Blundell, S.; Oleynichenko, A.V.; Garcia Ruiz, R.F.; Skripnikov, L.V.; Ohayon, B. Recent advancements in atomic many-body methods for high-precision studies of isotope shifts. *J. Phys. B At. Mol. Opt. Phys.* **2025**, *58*, 042001. [CrossRef]
10. Ekman, J.; Jönsson, P.; Godefroid, M.; Nazé, C.; Gaigalas, G.; Bieroń, J. RIS4: A program for relativistic isotope shift calculations. *Comput. Phys. Commun.* **2019**, *235*, 433–446. [CrossRef]
11. Lu, H.; Li, B.; Yang, M.; Dong, L.; Wang, Y.; Li, M.; Wu, L.; Li, J.; Jiang, J.; Dong, C.; et al. Isotope shifts due to the $1s^2 2s\,^2S_{1/2} \rightarrow 1s^2 2p\,^2P_{1/2,3/2}$ transitions of Li-like Th^{87+} ions. *Chin. Phys. B* **2025**, *34*, 073203. [CrossRef]
12. Sahoo, B.K.; Jönsson, P.; Gaigalas, G. Comparative analysis of Mg^+ properties using multiconfiguration Dirac–Hartree–Fock and relativistic coupled-cluster methods. *Phys. Rev. A* **2025**, *112*, 012809. [CrossRef]
13. Si, R.; Li, Y.; Wang, K.; Chen, C.; Gaigalas, G.; Godefroid, M.; Jönsson, P. GRASPG—An extension to GRASP2018 based on configuration state function generators. *Comput. Phys. Commun.* **2025**, *312*, 109604. [CrossRef]
14. Lennon, D.J.; Maíz Apellániz, J.; Irrgang, A.; Bohlin, R.; Deustua, S.; Dufton, P.L.; Simón-Díaz, S.; Herrero, A.; Casares, J.; Muñoz-Darias, T.; et al. Hubble spectroscopy of LB-1: Comparison with B^+ black-hole and Be^+ stripped-star models. *Astron. Astrophys.* **2021**, *649*, A167. [CrossRef]
15. Picciotto, A.; Margarone, D.; Velyhan, A.; Bellutti, P.; Krasa, J.; Szydlowsky, A.; Bertuccio, G.; Shi, Y.; Mangione, A.; Prokupek, J.; et al. Boron-proton nuclear-fusion enhancement induced in boron-doped silicon targets by low-contrast pulsed laser. *Phys. Rev. X* **2014**, *4*, 031030. [CrossRef]
16. Leblond, S.; Marqués, F.M.; Gibelin, J.; Orr, N.A.; Kondo, Y.; Nakamura, T.; Bonnard, J.; Michel, N.; Achouri, N.L.; Aumann, T.; et al. First Observation of ^{20}B and ^{21}B. *Phys. Rev. Lett.* **2018**, *121*, 262502. [CrossRef] [PubMed]
17. Jönsson, P.; Johansson, S.G.; Fischer, C.F. Accurate Calculation of the Isotope Shift and Hyperfine Structure in the Boron (B ii) Line at 1362 Angstrom. *Astrophys. J. Lett.* **1994**, *429*, L45. [CrossRef]
18. Liu, J.; Li, J.; Zou, H. Uncertainty evaluation of the isotope shift factors for $2s2p\,^{3,1}P^o_1$–$2s^2\,^1S_0$ transitions in B II. *Chin. Phys. B* **2017**, *26*, 023104. [CrossRef]
19. Cheng, Y.; Mitroy, J. Blackbody radiation shift of the B^+ clock transition. *Phys. Rev. A* **2012**, *86*, 052505. [CrossRef]
20. Crespo L'opez-Urrutia, J.R. The visible spectrum of highly charged ions: A window to fundamental physics. *Can. J. Phys.* **2008**, *86*, 111–123. [CrossRef]
21. Yerokhin, V.A.; M"uller, R.A.; Surzhykov, A.; Micke, P.; Schmidt, P.O. Nonlinear isotope-shift effects in Be-like, B-like, and C-like argon. *Phys. Rev. A* **2020**, *101*, 012502. [CrossRef]
22. Froese Fischer, C.; Godefroid, M.; Brage, T.; Jönsson, P.; Gaigalas, G. Advanced multiconfiguration methods for complex atoms: I. Energies and wave functions. *J. Phys. B At. Mol. Opt. Phys.* **2016**, *49*, 182004. [CrossRef]
23. Jönsson, P.; Godefroid, M.; Gaigalas, G.; Ekman, J.; Grumer, J.; Li, W.; Li, J.; Brage, T.; Grant, I.P.; Bieroń, J.; et al. An Introduction to Relativistic Theory as Implemented in GRASP. *Atoms* **2023**, *11*, 7. [CrossRef]
24. Li, Y.T.; Wang, K.; Si, R.; Godefroid, M.; Gaigalas, G.; Chen, C.Y.; Jönsson, P. Reducing the computational load–atomic multiconfiguration calculations based on configuration state function generators. *Comput. Phys. Commun.* **2023**, *283*, 108562. [CrossRef]
25. Sturesson, L.; Jönsson, P.; Froese Fischer, C. JJGEN: A flexible program for generating lists of *jj*-coupled configuration state functions. *Comput. Phys. Commun.* **2007**, *177*, 539–550. [CrossRef]
26. Kramida, A.; Ralchenko, Y.; Reader, J.; NIST ASD Team. *NIST Atomic Spectra Database*; Version 5.12; National Institute of Standards and Technology: Gaithersburg, MD, USA, 2024. Available online: https://physics.nist.gov/asd (accessed on 5 July 2026).
27. Nazé, C.; Verdebout, S.; Rynkun, P.; Gaigalas, G.; Godefroid, M.; Jönsson, P. Isotope shifts in beryllium-, boron-, carbon-, and nitrogen-like ions from relativistic configuration interaction calculations. *At. Data Nucl. Data Tables* **2014**, *100*, 1197–1249. [CrossRef]
28. Litzén, U.; Zethson, T.; Jönsson, P.; Kasten, J.; Kling, R.; Launay, F. Precision measurements and calculations in the B II spectrum: Wavelengths, isotope shifts, and oscillator strengths. *Phys. Rev. A* **1998**, *57*, 2477–2484. [CrossRef]
29. Wang, K.; Chen, Z.B.; Zhang, C.Y.; Si, R.; Jönsson, P.; Hartman, H.; Gu, M.F.; Chen, C.Y.; Yan, J. Benchmarking atomic data for astrophysics: Be-like ions between B II and Ne VII. *Astrophys. J. Suppl. Ser.* **2018**, *234*, 40. [CrossRef]

30. Fischer, C.F.; Brage, T.; Jönsson, P. *Computational Atomic Structure: An MCHF Approach*; Routledge: Abingdon, UK, 1997. [CrossRef]
31. Tong, M.; Jönsson, P.; Fischer, C.F. Convergence studies of atomic properties from variational methods: Total energy, ionization energy, specific mass shift, and hyperfine parameters for Li. *Phys. Scr.* **1993**, *48*, 446. [CrossRef]
32. Angeli, I.; Marinova, K.P. Table of experimental nuclear ground state charge radii: An update. *At. Data Nucl. Data Tables* **2013**, *99*, 69–95. [CrossRef]
33. Korol, V.A.; Kozlov, M.G. Relativistic corrections to the isotope shift in light ions. *Phys. Rev. A* **2007**, *76*, 022103. [CrossRef]
34. Jönsson, P.; Litzén, U.; Zethson, T.; Kling, R.; Launay, F. Wavelengths, isotope shifts, and oscillator strengths in B II at 1362 and 1624 Å. *Astrophys. J. Lett.* **1998**, *499*, L107–L109. [CrossRef]
35. Audi, G.; Wapstra, A.H.; Thibault, C. The AME2003 atomic mass evaluation: (II). Tables, graphs and references. *Nucl. Phys. A* **2003**, *729*, 337–676. [CrossRef]
36. Soria Orts, R.; Harman, Z.; Crespo L'opez-Urrutia, J.R.; Artemyev, A.N.; Bruhns, H.; González Martínez, A.J.; Jentschura, U.D.; Keitel, C.H.; Lapierre, A.; Mironov, V.; et al. Exploring Relativistic Many-Body Recoil Effects in Highly Charged Ions. *Phys. Rev. Lett.* **2006**, *97*, 103002. [CrossRef] [PubMed]

Disclaimer/Publisher's Note: The statements, opinions and data contained in all publications are solely those of the individual author(s) and contributor(s) and not of MDPI and/or the editor(s). MDPI and/or the editor(s) disclaim responsibility for any injury to people or property resulting from any ideas, methods, instructions or products referred to in the content.